Optimization of a dual-end readout bar-shaped scintillator detectors for Compton imaging

Cheng-Shuai Tian,[1] Jian Yang,[1,*] Guo-Qiang Zeng,[1,†] Xin-Yu Yang,[1] Hao-Wen Deng,[1] Chuan-Hao Hu,[1] and Chun-Di Fan[1]

[1] *College of Nuclear Technology and Automation Engineering, Chengdu University of Technology, Chengdu 610059, China*

Compton imaging enables high-sensitivity imaging of gamma radiation sources without collimation, making it useful for homeland security, nuclear decommissioning, and space science. This study proposes a position-sensitive bar-shaped detector used for Compton imaging. The bar-shaped scintillator detectors are arranged in a planar array, with signals read out from the dual end of the detector to reduce electronics channels. The detection system developed in this study with advantages of radiation hardness, high efficiency and low cost. A large sensitive volume of a 5 mm × 5 mm × 100 mm CsI(Tl) scintillator detector, with a light output of 56,000 photons/MeV, was used to verify position and energy resolution. Considering the surface roughness and reflectors, the experiment results indicate that the bar-shaped scintillators can achieve an average position resolution better than 5mm and 7.2%(FWHM) energy resolution at 662 keV. Therefore, a balance between position resolution and energy resolution can be achieved by the bar-shaped scintillators with few readout electronics. The imaging detection system of 80 cm^3 sensitive volume, constructed with bar-shaped scintillators, can be used for Compton imaging in an energy range of 250 keV to 3 MeV.

Keywords: Gamma-ray imaging; Position resolution; Readout electronics; Optical photon; Monte Carlo

I. INTRODUCTION

The gamma camera used for radioactive imaging has been widely applied in the fields of nuclear non-proliferation [1], nuclear emergency[2], medical imaging [3–5], environmental monitoring [6, 7], and space exploration [8–10]. Coded aperture imaging and Compton imaging are the two main gamma-ray imaging methods. Encoded aperture imaging is based on an aperture array projects radiation from sources at various angles onto the detector, forming distinct patterns that are decoded to reconstruct the image [11]. Coded aperture imaging exhibits superior angular resolution for incident gamma-rays with lower energy. For instance, the panoramic coded aperture gamma camera by Shifeng Sun achieves an angular resolution of 3.5° for a ^{137}Cs source [12]. However, the presence of the coded aperture blocks a portion of the gamma rays, reducing the detection efficiency. Moreover, high-energy gamma rays are difficult to absorb effectively by the mask, leading to blurred projections and decreased contrast. Consequently, for medium- to high-energy gamma rays, Compton imaging is more suitable, as it eliminates the need for collimators, enabling a wider field of view and higher detection efficiency [13]. Nowadays, various structures of Compton cameras have been proposed, such as monolithic detectors and multilayer detectors [14–16].

The monolithic detector is sensitive to all directions of incident gamma-ray to obtain a wide field of view, but it must have the 3-D position-sensitive capability to distinguish the depth of two energy depositions. Charles University used a CdTe detector with a Timepix3 chip to image ^{131}I, ^{137}Cs, and ^{22}Na sources from different directions. Due to the detector's thinness, filtering and deconvolution algorithms were applied to enhance image quality [17]. Tsinghua University built a Compton camera with a 3-D position-sensitive CZT detector to identify isotopes and locate ^{137}Cs sources, though with slightly inadequate angular resolution [18]. The approach using pixelated scintillators with SiPM or MPPC has also been proposed, in addition to semiconductor detectors [19]. Waseda University proposed a Compton camera with pixelated GAGG scintillators and MPPC arrays, achieving 7.8% energy resolution (FWHM) at 662keV and 8° angular resolution for ^{137}Cs source [20]. H. Lee et al. developed a Compton camera using the same scintillators, reducing radioactive background noise and making it suitable for compact platforms like drones[21]. J. Zhang simplified pixelated scintillator manufacturing using laser engraving, with MPPC readout on both sides to enhance spatial resolution [22]. Yifan Hu developed a gamma camera with a 4π field-of-view by interleaving GAGG(Ce) scintillator strips, eliminating collimators to improve portability and sensitivity [23]. Sophisticated electronics have been developed to read out the monolithic detector. However, due to the detector's limited size, the two interaction points of a Compton scattering event are in close proximity (respect to the detector's 3D spatial resolution), which ultimately leads to a deterioration in the angular resolution.

Multilayer detectors locate the scattering and absorption positions in different 2-D position-sensitive detectors to increase the number of effective imaging events. Shin Watanabe designed a Compton camera using a combination of 6 layers of double-sided silicon strip detectors (DSSD) and 3 layers of CdTe pixel detectors, achieving energy resolutions of 9.1 keV for 356 keV and 14 keV for 511 keV, as well as an angular resolution of 3.9° for 511 keV gamma-rays [24]. Although the multilayer structure improves imaging efficiency, it is more costly than the dual-layer structure. To reduce costs, the two-layer Compton imaging structure has become the mainstream. Ji-Peng Zhang built a camera using a dual-layer pixelated GAGG scintillator, achieving an energy resolution (FWHM) of 7.2% for 662keV gamma rays and an angular resolution of about 8° [25]. To increase the camera's sensitive detection volume, Ming Hao Dong built

* Corresponding author, yang_jian@cdut.edu.cn
† Corresponding author, zgq@cdut.edu.cn

a dual-layer Compton camera with enlarged LaBr3 detectors (10×10×10 and 10×10×5 mm^3), achieving 7° angular resolution for ^{137}Cs source [26]. To cover low-energy imaging, the High Efficiency Multimode Imager (HEMI) system from Berkeley, utilizes a dual-layer array with 1 cm^3 CZT detectors to achieve coded aperture imaging and Compton imaging [27].

As demand for gamma camera applications grows, various techniques have been proposed to enhance their practicality, such as increases the detector's sensitive volume [28], reduce the number of electronic channels [29], expand the field of view, or adapt to the single direction of far-field radiation imaging [30]. In addition to improvements in detector structure, a series of methods to enhance image performance have been proposed [31]. With the development of technology, researchers are increasingly focusing on improving the imaging efficiency of gamma cameras, reducing noise [32], and enhancing spatial resolution [33] and localization accuracy [34].

We propose a Compton camera design using a bar-shaped scintillator array. By analyzing the signals read out from the SiPMs coupled to both ends of each scintillator, the photon interaction position along the longitudinal axis can be reconstructed. This approach replaces the traditional array of small-volume scintillators, effectively increasing the sensitive volume of the Compton camera while reducing the number of electronics channels. The idea of using bar-shaped scintillators to determine the position of deposition was proposed as early as the 1970s and has been applied in high-energy astrophysics, such as the ZEBRA telescope and AGILE satellite [35–38], as well as in PET [39]. However, both the surface roughness of the scintillator and the reflective materials significantly affect its energy and position resolution. To achieve better energy and position resolution while increasing the detector's sensitive volume, we conducted simulations and experiments on the surface roughness and reflective materials of a 5mm×5mm×100mm CsI(Tl) detector. We investigated the impact of different reflective materials and surface roughness on these properties. The Compton camera utilizing this study significantly reduces the number of electronic channels compared to other Compton cameras with the same sensitive volume.

II. COMPTON IMAGING DETECTOR DESIGN

A. Structure of imaging detector

Compton imaging detectors require the ability of three-dimensional (3-D) position sensitivity. As shown in Figure 1(a), a typically double-layer structure was selected in this study. Generally, the first layer of the detector array serves as the scattering detector, while the second layer is the absorbing detector. Each layer of the detector array is composed of 16 parallel-arranged bar-shaped scintillator detectors, providing a 2-D position for the interaction. The detector system with 3-D position sensitivity is formed by using two layers of 2-D position detectors. The field of view for Compton imaging can be changed by adjusting the spacing between the two-layer detectors.

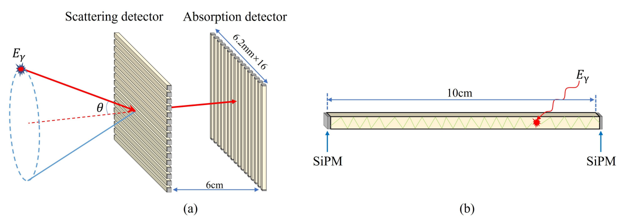

Fig. 1. (a) Compton imaging system with two layers of 2-D position detectors and (b) the minimum detector unit of bar-shaped scintillator detector.

In a two-dimensional planar array detector, the position resolution is discrete due to the discrete arrangement of the bar-shaped scintillator detectors. The continuous position segmentation along the axis of the bar-shaped scintillator detectors results in non-uniform position resolution. Orthogonal alignment of the detectors contributes to the uniformity of directional response.

The scattering detector with 2-D position sensitivity provides the position and energy deposition, (x_1, y_1, z_1, e_1), for the interaction point of Compton scattering, while the interaction position and energy deposition of the absorbed scattered photon, (x_2, y_2, z_2, e_2), is obtained by the 2-D position sensitive absorbed detector. Assuming that the electrons in the scattering process are initially at rest (i.e., their initial kinetic energy and motion are negligible), the expected energy of the scattered photons can be calculated using Equation (1). This energy calculation is based on the kinematics of Compton scattering. Subsequently, the deflection angle of the scattered photons, can be derived from Equation (1), as shown in Equation (2) [40]. Due to the limited spatial resolution of bar detectors, it is not possible to know the trajectories of the electrons produced in the scattering, so that the photon's directions of incidence can only be reconstructed as a conical surface representing all directions compatible with the two photon interaction positions and their energy deposits. This conical surface is known as the Compton cone or the back-projection cone. By detecting a large number of Compton scattering events, the position of the radiation source can be located by the intersecting Compton cones[41].

$$E' = \frac{E_0}{1 + (E_0/m_e c^2)(1 - \cos\theta)} \tag{1}$$

$$\cos\theta = 1 - \frac{m_e c^2 (E_0 - E')}{E_0 E'} \tag{2}$$

where E_0 is the energy of the incident photon, E' is the energy of the scattered photon, θ is the Compton scattering angle, m_e is the rest mass of the electron, and c is the speed of light.

To increase the sensitive volume of the detector system, a large volume bar-shaped scintillator coupled with two SiPMs

on the end faces of the detector is shown in Figure 1(b) as its minimum detection unit. When radiation interacts with the scintillator detectors, the generated scintillation photons propagate toward the two ends of the detector. Due to the interface reflection and self-absorption in scintillator, scintillation photons will be reduced with an exponential decay. This feature facilitates the position reconstruction of the interaction within the detector by measuring the pulse signal amplitudes from the two SiPMs along the bar's main axis direction. This method makes the bar-shaped scintillator has one-dimensional position resolution capability. Each SiPM is equipped with its own dedicated electronic readout channel to reduce electronic noise while increasing position and energy resolution. Some methods for improving the spatial resolution and spectroscopy of bar-shaped scintillators have been applied in the ZEBRA telescope and the AGILE, providing valuable insights for this study[37, 38].

In the experiments, to alter the roughness of the bar-shaped scintillator surface, we use sandpaper with similar roughness to uniformly sand the surface, ensuring the consistency of the scintillator surface. The reflective layer was applied by two methods: one involved wrapping the scintillator with Teflon tape, while the other involved placing the scintillator bar in a mold, pouring TiO_2 slurry over its surface, and then placing the mold in a vacuum environment to eliminate air bubbles from the slurry. After curing, the TiO_2 layer was ground to a thickness of 0.5 mm. These optimizations contribute to improved signal quality and measurement accuracy. Ultimately, this imaging structure allows a single-layer array detector with 2D position sensitivity to have a larger sensitive volume while using fewer electronic channels. To increase the sensitive volume of Compton detectors, consider using two or more layers of array detectors. This modular design allows for more flexibility in adjusting the sensitive volume while also reducing the complexity of the electronics. When choosing a detector, it is critical to consider the energy resolution of the scintillator detector and the available manufacturing technology.

B. Monte Carlo modeling

This work describes a Compton camera design that employs position-sensitive bar-shaped scintillators as the minimum detection unit. However, the surface parameters of the scintillator have a significant impact on its optical properties. For example, two important parameters of Compton camera, namely position reconstruction accuracy and energy resolution, are sensitive to surface roughness and reflective layer material [42]. Deservedly, we can optimize its position resolution capabilities by adjusting the surface parameters of the scintillator and choosing appropriate reflective materials. To validate the feasibility of this design, we created detailed models of the scintillator and the minimum detection unit using the Monte Carlo simulation software Geant4. We modeled and simulated several representative surface parameters and reflective layer material to evaluate their effects on the position and energy resolutions, which can provide some insights into optimizing the detector's performance based on the chosen surface characteristics.

First, based on the structure shown in Figure 1(b), we constructed a simulation model of a basic unit using Geant4. Next, we employed the optical photon physics model in the Geant4 software package to simulate the fluorescence photons produced in the scintillator and the internal optical characteristics of the scintillator [43]. To closely approximate real-world conditions, we adopted the Unified Model for the optical simulation. This model is particularly suitable for complex optical surfaces and allows flexible adjustments for parameters such as specular spike, specular lobe, diffuse lobe, reflection, and backscattering. These parameters offer high flexibility, with the sum of the Specular Spike, Specular Lobe, and Diffuse Lobe always equal to 1. By adjusting the ratios of these three parameters, we can effectively change the surface roughness and simulate different optical behaviors. We selected the Dielectric-Dielectric and Dielectric-Metal boundary types to represent Teflon-wrapped and TiO_2-coated surfaces, respectively. By precisely configuring these parameters, we can accurately simulate the optical behavior of various material surfaces, facilitating more in-depth research.

It is important to consider a scintillator of high light yield. To meet these requirements, a commonly used CsI(Tl) scintillator was chosen for simulation studies due to its high scintillation efficiency and low intrinsic background radiation. The fluorescence efficiency of the CsI (Tl) scintillator is about 56000/MeV, the decay time is about 1020 ns, the average emission wavelength is 550 nm. The photon detection efficiency (PDE) of the SiPM for light at this wavelength is approximately 20%. To reduce simulation time, the SiPM's photon detection efficiency (PDE) was set to 100%. This adjustment simplifies simulation without compromising the accuracy of the results.

To increase the detector's sensitive volume and enhance imaging sensitivity, we need to maximize the cross-sectional area of the bar-shaped scintillator. SiPMs with larger light-sensitive areas are selected to achieve this goal. Currently, commercially available SiPMs with large light collection areas, typically around 6×6 mm^2 , include the EQR20 11-6060D-S from Novel Device Laboratory, S13360-6025PE from Hamamatsu, ARRAYC-60035 from onsemi, and AFBR-S4N66P014M from Broadcom. To collect photons emitted from both ends of the bar-shaped scintillator, we selected scintillators with a cross-sectional area of 5×5 mm^2 and a reflective material layer thickness of 0.5 mm. To ensure accurate measurement of the interaction depth within the scintillator, we chose bar-shaped scintillators with a size of $5\times5\times100$ mm^3 . We propose to construct a double-layer Compton camera using 32 bar-shaped scintillator detectors of this dimension, with a sensitive detection volume of 80 cm^3 . A larger sensitive volume can enhance imaging efficiency, meaning that more events suitable for imaging can be obtained within the same period, thereby reducing the imaging time.

To study the effects of different surface roughness under the same reflective layer, and the impact of various reflective layers with the same roughness on the final energy res-

olution and position resolution of the bar-shaped scintillator, we used Teflon and (TiO_2) as reflective materials. Consider whether the scintillator surface is rough or not, we modeled and analyzed four typical characteristics, as shown in Figure 2. It should be noted that when Teflon is used as a reflective material to wrap the scintillator, the reflective material and the crystal surface typically do not fit tightly, usually creating small air gaps. As shown in Figure 2(a) and 2(b), these air gaps can affect experimental results. In contrast, when a reflective coating is applied to cover the crystal surface, the reflective material makes tight contact with the scintillator surface. As illustrated in Figure 2(c) and 2(d), there are no air gaps between the two surfaces. This difference is crucial in experimental design, as the air gaps can alter the optical properties of the scintillator, thereby affecting the performance of the detector. Through simulation analysis of these characteristics, we can gain a better understanding of how surface roughness and reflective layer materials affect the performance of the bar-shaped scintillator.

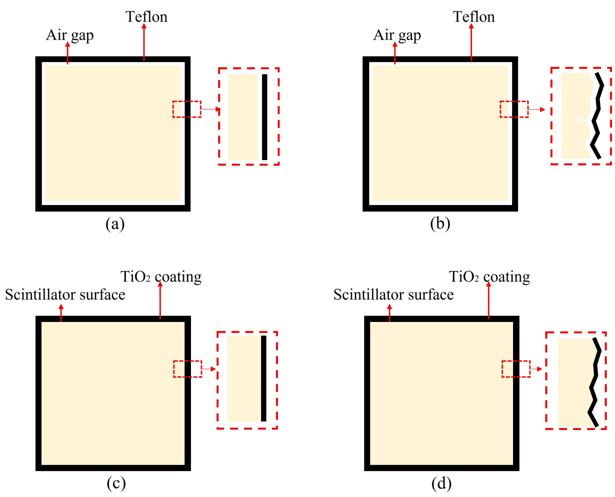

Fig. 2. (a) The scintillator is wrapped around Teflon, so there is an air gap and has a polished surface. (b) The scintillator is wrapped around Teflon, and has a rough surface. (c) The scintillator is coated with titanium dioxide, so there is no air gap and has a polished surface. (d) The scintillator is coated with titanium dioxide, and has a rough surface.

In the simulation process, a gamma ray source with an energy of 662 keV is used. The source is positioned 40 cm away from the central axis of the scintillator, with its emission direction aligned toward the scintillator. By moving the radiation source, a uniform irradiation scenario is simulated. The G4StepAction function is employed to monitor the type of particles produced in each step and the energy deposited by the radiation. In Geant4, each individual particle trajectory is assigned a unique track ID. For photons, once generated, Geant4 assigns a track ID to the photon. This ID enables the tracking of the photon's path throughout the simulation, including its propagation, interactions with matter, and eventual disappearance. When combined with the G4StepAction function, it allows for the simulation and tracking of the total number of photons generated within the scintillator and the number of photons detected by the dual-ended SiPMs. This data provides insights into photons propagating through the scintillator and helps in evaluating the energy and position resolution of the detector based on varying surface and reflective layer parameters.

The Compton imaging system consists of two-layer of array detectors. Each layer consists of 16 detection units, each unit with a center-to-center spacing of 6.2 mm. The resulting single-layer array detector approximates a square configuration, as shown in Figure 1(a). Additionally, the spacing between the two detector layers can be adjusted as required to modify the imaging field of view (FOV). The default spacing between the two array detectors is 60 mm, which allows for a larger field of view. With this configuration, the system has a total of 32 detection units, yielding 64 electronic channels. The effective sensitive volume of the detector is 80 cm^3.

III. SIGNAL PROCESSING AND EVENT RECONSTRUCTION

A. Event reconstruction method

To determine the deposition location and energy of rays in a bar-shaped scintillator, an appropriate depth of Interaction (DOI) reconstruction method is required. Currently, the DOI reconstruction methods used with dual-end readout scintillator detectors primarily fall into two categories: the time-of-flight method [44] and the amplitude-ratio method [45]. The time-of-flight method uses the time difference between the pulses received at the two ends of the scintillator to determine the location of the radiation interaction in the scintillator . This method has been applied in the balloon-borne Compton telescope [46]. However, this method requires high accuracy and high sampling rates from electronics, and is more suitable for longer scintillators. Adopting this method would increase the complexity and cost of the electronics. The amplitude-ratio method for DOI reconstruction by using the ratio of the number of photons emitted from the two ends of the scintillator to determine the interaction depth within the scintillator. This method eliminates the need for high time resolution and high sampling rates in the electronics, effectively reducing the complexity and cost of the electronics. Given these considerations, the proposed design uses the amplitude-ratio method for DOI reconstruction.

The reconstruction method of amplitude-ratio analysis is as follows. When the bar-shaped scintillator has the same cross-sectional area shape, such as rectangular or cylindrical, and there is no light guide between the scintillator and the photodetector. When the surface of the scintillator exhibits uniform roughness, under ideal conditions, the scintillation photons produced within the scintillator are transmitted to dual-end in an approximate exponential attenuation. The attenuation distance l_0 is related to scintillator size, surface roughness, and reflector. The exponential decay behavior is critical for determining the depth of interaction (DOI) within the scintillator by comparing the relative pulse amplitudes from

both ends of the detector.

Assuming that when the interaction position and the energy deposition position are in the middle of the bar-shaped scintillator, the DOI (Depth of Interaction) value, Z_{DOI} is 0, and the length of the scintillator is L. If an incident particle deposits energy at a position Z_{DOI} within the scintillator and generates N photons, the number of photons collected at the left and right ends can be calculated as follows:

$$N_{left} = 0.5\varepsilon N e^{\frac{-(L/2+Z_{DOI})}{l_0}} \tag{3}$$

$$N_{right} = 0.5\varepsilon N e^{\frac{-(L/2-Z_{DOI})}{l_0}} \tag{4}$$

Where ε is the detection efficiency of the photodetector, defined as the ratio of the number of photons detected by the detector to the number of photons incident on the detector. And l_0 is the exponential attenuation length for the photons within the scintillator.

To evaluate positioning accuracy, we define the parameter F as the ratio of the number of photons emitted from one end to the total number of photons emitted from both ends:

$$F = \frac{N_{right}}{N_{right} + N_{left}} \tag{5}$$

By substituting formula (3) and (4) into formula (5), we get:

$$Z_{DOI} = -\frac{l_0}{2} \ln\left(\frac{1}{F} - 1\right) \tag{6}$$

By using the error propagation formula:

$$\sigma^2_{\mathrm{DOI}} = \left(\frac{\partial Z_{\mathrm{DOI}}}{\partial F}\right)^2 \sigma^2_{\mathrm{F}} \tag{7}$$

In the formula:

$$\frac{\partial Z_{\mathrm{DOI}}}{\partial F} = \frac{l_0}{2F(1-F)} \tag{8}$$

Since N_{left} and N_{right} are random variables obeying Poisson distribution, their variances are:

$$Var(N_{right}) = N_{right} \quad Var(N_{left}) = N_{left} \tag{9}$$

Based on the variance formula for ratios:

$$\sigma^2_F = \frac{N^2_{\mathrm{right}} N_{\mathrm{left}} + N^2_{\mathrm{left}} N_{\mathrm{right}}}{(N_{\mathrm{left}} + N_{\mathrm{right}})^4} \tag{10}$$

Therefore, the positioning accuracy can be obtained by measuring the fluctuation of parameter F :

$$\sigma^2_{DOI} = -\frac{l_0^2}{2\varepsilon N}\left(e^{\frac{L/2+Z_{DOI}}{l_0}} + e^{\frac{L/2-Z_{DOI}}{l_0}}\right) \tag{11}$$

According to formulas (3) and (4), the geometric mean of the read signal at dual-end is proportional to the total number of photons generated and is independent of the depth of interaction. Thus, the energy resolution can be measured.

$$\sqrt{N_{left}N_{right}} = \varepsilon N e^{-\frac{L}{l_0}} \propto N \propto E_{deposition} \tag{12}$$

Thus, each minimum detection unit is equipped with its signal readout circuit. The method described previously can be used to reconstruct position by analyzing the signal amplitude. Additionally, the signal amplitude can be used to determine the energy deposited by radiation in the bar-shaped scintillator, allowing for energy measurement.

B. Simulation results and experimental parameter selection

After building the simulation model for the minimum detection unit in Geant4, perform a simulation and comparison analysis on the four typical scenarios shown in Figure 2. This will help in the identification of the characteristics suitable for position and energy reconstruction in bar-shaped scintillators, which will be validated experimentally.

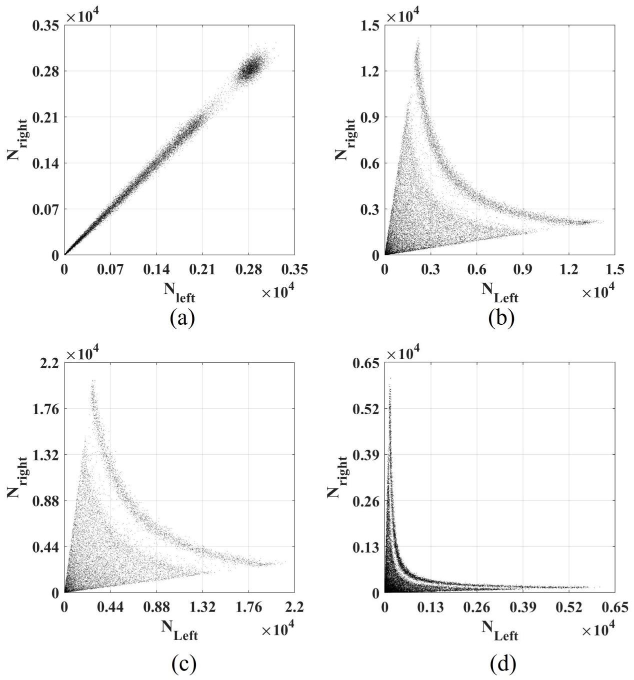

Fig. 3. Simulation results of the light intensity distribution for the scintillator (a) wrapped with Teflon on its polished surface and (b) Teflon on its rough surface, while (c) coated with TiO_2 to its polished surface and (d) TiO_2 on its rough surface.

The simulation recorded the incident position of the gamma rays and number of photons emitted from dual-ends of the scintillator. The number of photons emitted from both ends of the scintillator in the four simulations are plotted as a scatter plots, as shown in Figure 3. And the plot in Figure

4 shows the parameter F versus the reconstructed interaction position along the bar's main axis.

The simulation results indicate that, under the conditions shown in Figure 3(a), photon attenuation within the scintillator is minimal, resulting in no significant difference in the number of photons emitted from both ends. This leads to poor position resolution for the strip-shaped scintillator. In contrast, the results in Figure 3(d) show a high degree of photon attenuation within the scintillator, making it difficult for photons generated in the middle to exit from both ends, which deteriorates the energy resolution of the strip-shaped scintillator. Meanwhile, the results shown in Figures 3(b) and (c) reveal a good balance between energy and position resolution.

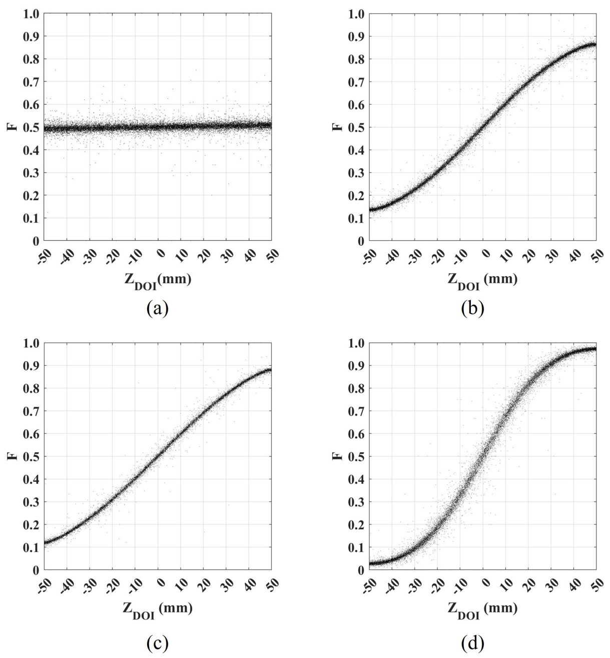

Fig. 4. Simulation results of the parameter F distribution for the scintillator processed the same as Fig.3.

To investigate the impact of scintillator surface parameters on energy resolution in these four typical scenarios, the method described in Section 3.1 was used to calculate the energy resolution based on the number of photons emitted from each end. The results are shown in Table 1.

TABLE 1. Energy resolution of four simulation results

Condition	(a)	(b)	(c)	(d)
FWHM	7.77%	10.49%	7.90%	44.14%

Based on the above-given simulation results, we can draw the following conclusions:

1. According to the results shown in Figures 4(a), when the scintillator surface is polished and wrapped with Teflon reflective material, the parameter F remains relatively constant as the DOI varies. This might be due to the high probability of total internal reflection at the medium's surface, resulting in no discernible difference in the number of photons emitted from both ends. This situation is unfavorable for position reconstruction. However, as illustrated in Figure 4(b), when the scintillator surface is rough, the F varies monotonically and noticeably with the DOI. This characteristic is beneficial for position resolution capability. At the same time, by comparing Figures 3(a) and 3(b), when the surface roughness increases, energy resolution deteriorates to some extent.

2. According to the results shown in Figures 4(c), when the scintillator surface is polished and coated with $\mathrm{TiO_2}$, the coating is tightly adhered to the scintillator surface. The parameter F exhibits a clear and monotonic variation with the DOI, indicating good position and energy resolution capabilities. This may be because the $\mathrm{TiO_2}$ coating has a certain granularity, which increases the probability of diffuse reflection of light on the surface of the medium. However, as shown in Figure 4(d), when the scintillator surface becomes rougher, diffuse reflection increases, resulting in a broader range of parameter F values that no longer follow a monotonic trend. As shown in Figure 3(d), this can affect both position reconstruction and energy resolution. Increased surface roughness may reduce energy resolution due to additional scattering and reflections, complicating position and energy determinations.

3. According to the results shown in Figures 3(b) and 3(c), it can be seen that the scintillator has position and energy resolution when the scintillator surface is polished and coated with $\mathrm{TiO_2}$ or scintillator surface is rough and wrapped with Teflon.

However, under the conditions shown in Figure 3(c), the number of photons emitted from both ends is significantly higher than under the conditions in Figure 3(b), which is more favorable for reconstructing energy and position information.

In order to achieve the conditions described in Figure 3(b), the bar-shaped scintillator require surface roughening and wrapping with a reflective material. In this process, it is challenging to ensure the uniform contact between the scintillator surfaces and Teflon.

The above-described simulations only validated the trend-based changes caused by varying surface parameters and reflective layer materials. In addition, changes in factors like scintillator surface roughness, refractive index, and reflection efficiency can influence the number of photons emitted from both ends of the scintillator, and further affects the pulse amplitude of the SiPM output. Therefore, the simulation model must be adjusted following experimental results.

IV. EXPERIMENTAL RESULTS AND DISCUSSION

A. Hardware system verification

To experimentally validate the simulation results, a corresponding electronic hardware system was established. The hardware system must meet multi-channel and high-precision data acquisition requirements. The system includes a preamplifier readout circuit which scheme is shown in Figure 5(a).

The fixed framework and the circuit module in the blue box on the left, which scheme is shown in Figure 5(b). A four-channel high-speed waveform data acquisition card (DAQ), as shown in Figure 5(c). These components together form a comprehensive system for capturing and analyzing the signal data. The fixed frame is designed to hold three CsI(Tl) scintillators simultaneously. In the actual experiments, to minimize the impact of electronic measurement errors, a consistent set of electronic devices was utilized. Furthermore, repeated measurements were performed with different scintillator bars. This approach effectively mitigates experimental deviations caused by electronic errors, thereby improving the reliability and accuracy of the collected data.

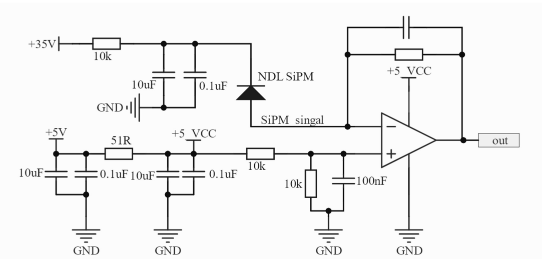

(a)

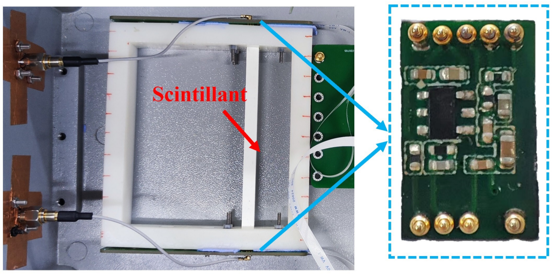

(b)

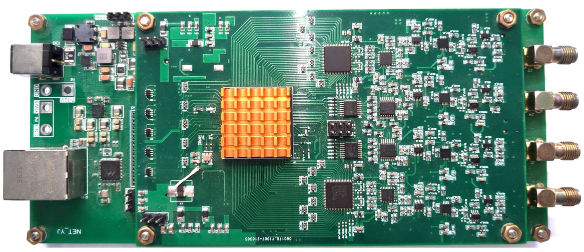

(c)

Fig. 5. (a) Readout electronics, (b) Fixed frame and Circuit module, (c) Data Acquisition Card

To ensure that photons emitted from dual-end of the scintillator are collected as effectively as possible by the SiPMs, we selected unique Epitaxial Quenching Resistor (EQR) SiPMs from Novel Device Laboratory (NDL). These SiPMs have several advantages, including a compact structure, high-density microcells, a wide dynamic range, high detection efficiency, a fast response time, excellent time resolution, insensitivity to ambient temperature, and radiation resistance [47].

The circuit shown in Figure 5(a) is used to ensure the stability of the SiPM output signals and reduce distortion. The anode of the SiPM is directly coupled to the input of the charge-sensitive preamplifier, ensuring that all the charge output from the SiPM is collected. However, this design can be affected by the SiPM's dark current, which may impact the precision of the output signal. In the actual measurement process, it is necessary to adjust the RC parameters for different scintillators to achieve better energy resolution. This approach helps to maintain signal integrity while optimizing the performance of the SiPM-based detection system. Table 2 shows the value ranges of some SiPM features.

TABLE 2. SiPM features

Type	EQR20 11-6060D-S
Effective Pitch	20μm
Element Number	1$\times$1
Active Area	6.24$\times$6.24 mm^2
Micro-cell Number	97344
Terminal Capacitance	397pF
Breakdown Voltage (V_B)	27.2V$\pm$1 V
Maximum operation voltage(V_m)	34.7$\pm$1.6 V
Recommended Operation Voltage	V_B + 5V
Temperature Coefficient for V_B	24.8 mV/°C
Peak PDE @ 420nm	47.8%
Gain	8.0$\times$ 10^5
Dark Count Rate (DCR)	150 kHz / mm^2 (Typical) 450 kHz / mm^2 (maximum)

The circuit shown in Figure 5(a) was made into a minimum basic detection circuit module depicted in the blue box on the left of Figure 5(b). The preamplifier and SiPM are mounted on the same PCB to reduce signal transmission distance and maintain signal quality. These components are coupled to the two end faces of the bar-shaped scintillator shown in Figure 5(b), with the signal output taken through coaxial cables. The pulse signals from the SiPMs at two ends of the scintillator are captured using the 4-channel high-speed waveform acquisition card shown in Figure 5(c). This acquisition card has excellent signal processing capabilities. The ADC on the card has a 16-bit resolution and an 80 MHz sampling rate, ensuring signal fidelity during sampling. After the high-speed ADC samples the signal, the data including channel number, timestamp, and raw waveform are processed and packaged within an FPGA, and then sent to computer for processing and display through Ethernet interface. The hardware gain, DC offset, and trigger threshold of the acquisition card can be adjusted through the upper computer, allowing for the flexible selection of optimal parameters to achieve the best signal-to-noise ratio.

The original pulse data is transmitted to the upper computer by a network transmission interface. Because of the captured pulse signals have a typical exponential decay pattern, digital filtering with the trapezoidal shaping algorithm is used to improve the accuracy of pulse amplitude measurements. This method not only filters out high-frequency noise but also al-

lows for precise amplitude extraction, which is useful for the subsequent analysis. The device shown in Figure 5(b) was placed in a fully light-tight metal shield box. In the experiment, the energy resolution of the bar-shaped scintillator was first tested using an uncollimated ^{137}Cs source. Subsequently, the source was collimated using a collimator to measure the position resolution at different points. This controlled environment helps to ensure accurate measurements while also reducing interference from external factors.

According to the simulation results in Section 3.2, we selected four CsI(Tl) scintillators with dimensions of $5\times5\times100$ mm^3 for experimental verification, and applied the following four experimental conditions: (a) Polished scintillator wrapped with Teflon; (b) Polished scintillator coated with TiO_2; (c) Scintillator surface with roughness of 800 mesh, wrapped with Teflon; (d) Scintillator surface with roughness of 800 mesh, coated TiO_2.

We conducted preliminary tests on the four selected scintillators. The scintillators were fixed using the frame shown in Figure 5(b), and uniformly irradiated with a ^{137}Cs radiation source at a distance of 40 cm. The signal amplitudes read by the SiPMs at both ends were recorded and plotted as a scatter plot, as shown in Figure 6. Based on the preliminary test results, the signal amplitude scatter plots from the SiPMs at both ends of the four selected scintillators closely match the simulation results.

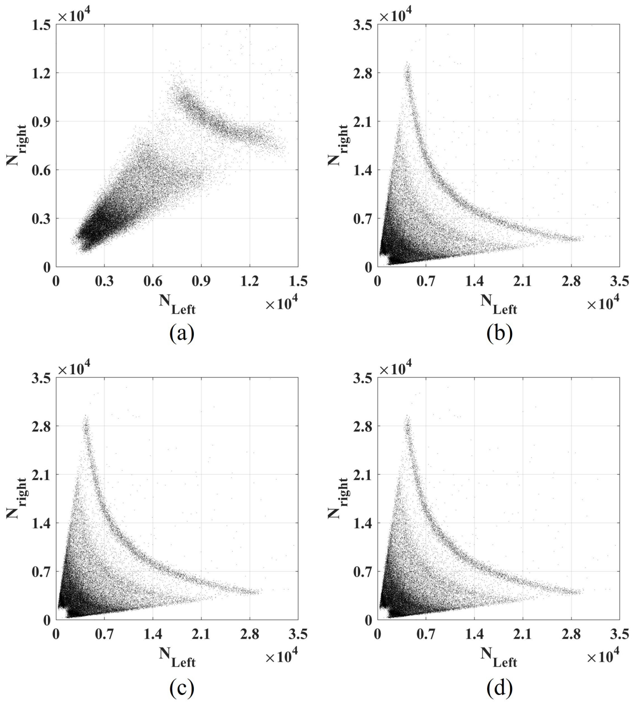

Fig. 6. Pulse amplitude output from the SiPMs at both ends for the scintillator: (a) polished with Teflon, (b) polished with TiO_2, (c) 800 mesh rough with Teflon, and (d) 800 mesh rough with TiO_2.

B. Performance measurement

To evaluate the position resolution of the scintillators, a collimated radioactive source was used to measure multiple points on the scintillator, as shown in Figure 7(a). To ensure the accuracy of the collimation measurement, the midpoint of the bar-shaped scintillator was taken as the reference point ($Z_{\mathrm{DOI}} = 0$). Five measurement points were evenly spaced on both sides, resulting in a total of 11 measurement points for collimated measurements.The experimental setup, shown in Figure 6(b), includes two lead bricks spaced 3 mm apart to collimate the ^{137}Cs source, and a guide rail was employed to slide the source, ensuring measurement accuracy.

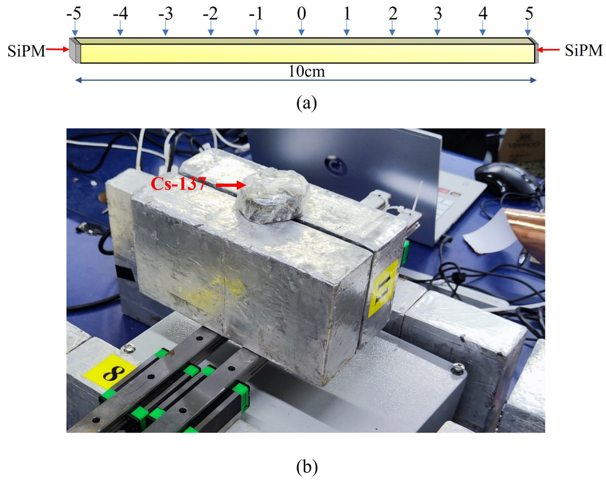

Fig. 7. (a) Test point and (b) testing device.

The scatter plot of the collimation measurements is summarized, and the data corresponding to the full-energy peak are selected to calculate the position resolution. Taking the bar-shaped scintillator is under experimental condition (b) as an example, the scatter plot of the eleven measurement points is shown in Figure 8(a). The fitted diagram of parameter F-value of the remaining points is shown in Figure 8(b).

Following the same approach, the measurement data of the other three bar-shaped scintillators were processed, and the parameters F and Z_{DOI} of the four measurements were fitted using Equation 6, as shown in Figure 9.

The results shown in Figure 9 indicate that under experimental condition (a), the position resolution of the bar-shaped scintillators is relatively poor. Under experimental condition (b), the distribution of parameters F and Z_{DOI} exhibits an approximately linear relationship, and the position resolution demonstrates good consistency. Under experimental condition (c), the position resolution near the two ends of the scintillator slightly decreases, but the overall performance remains within an acceptable range. In contrast, under experimental condition (d), the distribution of parameters F and Z_{DOI} shows a nonlinear relationship, and the position resolution error is larger near the two ends of the scintillator, leading to uneven overall position resolution.

According to the measurement results in Figure 9, when

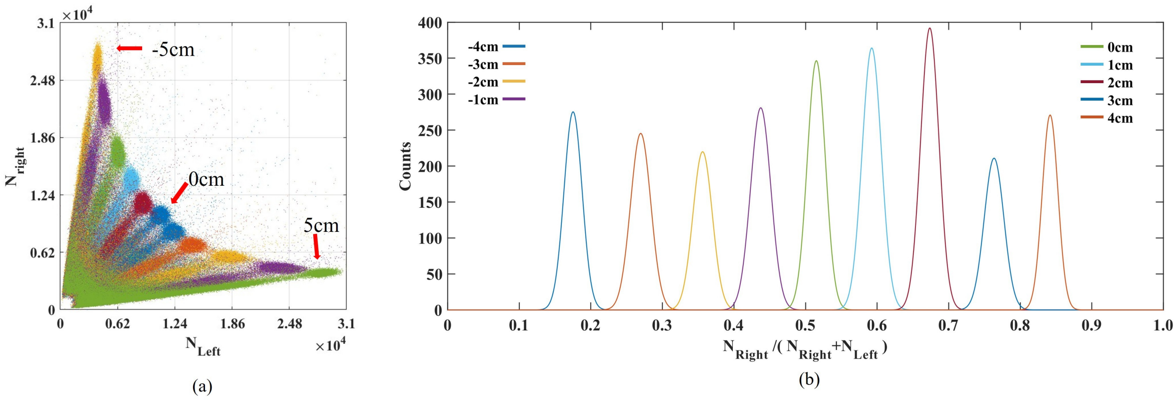

Fig. 8. (a) scatter plot of scintillation photons readout at the two-bar end for each gamma ray interaction at different source position and (b) different test point location resolution.

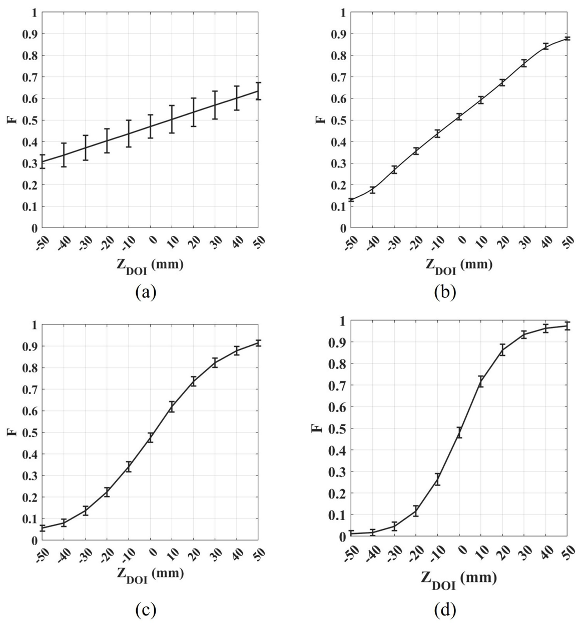

Fig. 9. Distribution of Parameter F under four conditions: (a) polished with Teflon, (b) polished with TiO_2, (c) 800 mesh rough with Teflon, and (d) 800 mesh rough with TiO_2.

the bar-shaped scintillator is under condition (b) with a polished surface and coated with a TiO_2 reflective coating, the scintillator achieves a position resolution of better than 5 mm. Therefore, the energy resolution at different test points of this scintillator was further analyzed. Figure 10(a) shows the energy spectra for half of the eleven measurement points. It can be observed that when the measurement points are near the edge of the scintillator, the energy spectra widen significantly. Figure 10(b) shows the energy resolution at each point, and it can be seen that the energy resolution at both ends of the scintillator bar decreases, but the average energy resolution remains 7.2%.

C. Analysis and discussion

The estimated energy resolution and position resolution for the four bar-shaped scintillators, as well as the fitting functions between parameters F and the interaction position, are presented in Table 3.

Based on the experimental results, we can draw the following conclusions:

1. According to Figure 6(a), when the scintillator has a smooth surface and is wrapped in Teflon reflective material, its position resolution is reduced, which is consistent with the simulation results. By comparing Figures 6(a) and 6(c), the reflective materials coated in both are Teflon, the scintillator exhibits some position resolution when its surface is rough. It shows that the position and energy resolution of bar-shaped scintillator can be improved by selecting suitable surface roughness when the scintillator is wrapped by Teflon.

2. According to Figure 6(b), when the scintillator has a smooth surface and is coated with TiO2, it exhibits good energy resolution and some position resolution. However, as the surface roughness increases, the energy resolution decreases, which is consistent with the simulation results. By comparing Figures 6(b) and 6(c), we can see that, while both scenarios exhibit some energy and position resolution, the pulse amplitude at both ends of the scintillator is significantly smaller in the condition shown in Figure 6(c).

In summary, to achieve good energy resolution and position resolution for bar-shaped scintillators, two typical surface characteristics can be selected: a polished surface covered with a TiO_2 reflective coating and a rough surface wrapped with Teflon reflective material. When the scintillator surface is wrapped with reflective material, changes in surface roughness can have a significant impact on the position resolution and energy resolution. Considering the difficulty of ensuring consistency among multiple detectors when the reflective material is wrapped around the scintillator surface, it is recommended to fully polish the surface and use TiO_2 coating as the reflective material.

Table 4 compares the key advantages of the detection sys-

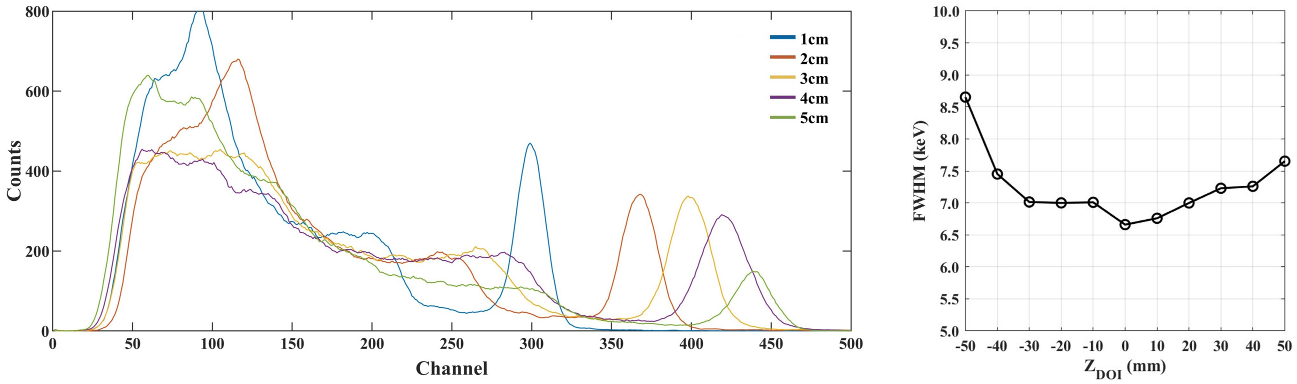

(a) (b)

Fig. 10. (a) Energy resolution of different test points and (b) global energy resolution.

TABLE 3. Comparison of energy resolution, position resolution, and F with respect to interaction position for four Surface Types

	Surface type	Reflector	FWHM	Position resolution	F as a Function of Z_{DOI}
(a)	polished	Teflon	10.18%	34mm	$Z_{DOI} = -72.58 \ln\left(\frac{1}{F} - 1\right)$
(b)	polished	TiO_2	7.21%	5mm	$Z_{DOI} = -26.87 \ln\left(\frac{1}{F} - 1\right)$
(c)	Roughness 800 mesh	Teflon	20.67%	8mm	$Z_{DOI} = -18.08 \ln\left(\frac{1}{F} - 1\right)$
(d)	Roughness 800 mesh	TiO_2	No clear photopeak	16mm	$Z_{DOI} = -10.47 \ln\left(\frac{1}{F} - 1\right)$

tem proposed in this paper with data reported in the literature, highlighting the unique characteristics of different Compton camera designs.

V. CONCLUSIONS

This study describes a structure for constructing a Compton camera using a position-sensitive bar-shaped scintillator array, which utilizes the pulse amplitude read out from dual-end of the scintillator to reconstruct the energy and position of gamma rays deposited within the scintillator. This method has several advantages over traditional Compton cameras built with small-volume scintillator arrays, such as a larger sensitive volume and fewer electronic channels. The Geant4 simulation software was used for modeling and simulation to optimize the surface parameters of the bar scintillator for better energy and position resolution of the minimum detection unit. The results showed that the best position and energy resolution was achieved when the surface of the strip CsI(Tl) scintillator was smooth and coated with a TiO_2 reflective layer. According to the simulation results, the CsI(Tl) scintillator has an average energy resolution of 7.2% at 662 keV energy and a position resolution of better than 5 mm. Most importantly, this study indicates that constructing a Compton camera using position-sensitive strip scintillators is feasible.

VI. AUTHORSHIP CONTRIBUTION STATEMENT

Cheng-Shuai Tian: Data curation, methodology, validation, Writing - original draft. **Jian Yang:** Conceptualization, funding acquisition, Supervision, Writing - review & editing. **Guo-Qiang Zeng:** Project administration, Supervision. Xin-Yu Yang: Investigation, Visualization. **Hao-Wen Deng:** Formal analysis, Validation. **Chuan-Hao Hu:** Supervision, Writing - review & editing. **Chun-Di Fan:** Validation, Formal analysis.

TABLE 4. Parameter Comparison of This System and Other Structural Compton Cameras

Research from	This study	University of Michigan [48]	Chinese Academy of Sciences [22]	Institute of High Energy Physics [25]	Berkeley University [27]
Detector structure	Bar-shaped CsI(Tl) scintillator array	Single 3D position-sensitive CZT detector	3D position YSO detector	Two-layer pixelated GAGG:Ce	CZT detector array
Sensitive volume	$80cm^3$	$6cm^3$	$19.6cm^3$	$38.4cm^3$	$96cm^3$
Energy resolution	7.2%@662keV	<1%@662keV	9.3 %@662keV	8.5 %@662keV	<2%@662keV
Position resolution	<5mm	1.72mm	3mm	2.2mm	>10mm
Characteristic	Large sensitive volume and lower cost	High energy resolution	4π imaging field of view	High position resolution	High detection efficiency

[1] Y. Shikaze, Y. Nishizawa, Y. Sanada et al., Field test around Fukushima Daiichi nuclear power plant site using improved Ce:Gd3(Al,Ga)5O12 scintillator Compton camera mounted on an unmanned helicopter. J. Nucl. Sci. Technol. **53**(12), 1907–1918 (2016). doi:10.1080/00223131.2016.1185980

[2] T. Lee, H. Lee, Y. Kim et al., Estimation of Compton imager using single 3D position-sensitive LYSO scintillator: Monte Carlo simulation. J. Korean. Phys. Soc. **71**(2), 70–76 (2017). doi:10.3938/jkps.71.70

[3] Z.Y. Yao, Y.S. Xiao, J.Z. Zhao, Dose reconstruction with Compton camera during proton therapy via subset-driven origin ensemble and double evolutionary algorithm. Nucl. Sci. Tech. **34**(4) (2023). doi:10.1007/s41365-023-01207-1

[4] P. Rossi, G. Baldazzi, A. Battistella et al., Design and performance tests of the calorimetric tract of a Compton Camera for small-animals imaging. Nucl. Instrum. Meth. A. **628**(1), 430–433 (2010). doi:10.1016/j.nima.2010.07.018

[5] Q. Ye, P. Fan, R. Wang et al., A high sensitivity 4π view gamma imager with a monolithic 3D position-sensitive detector. Nucl. Instrum. Meth. A. **937**, 31–40 (2019). doi:10.1016/j.nima.2019.05.022

[6] Y.S. Kim, J.H. Kim, H.S. Lee et al., Development of Compton imaging system for nuclear material monitoring at pyroprocessing test-bed facility. J. Nucl. Sci. Technol. **53**(12), 2040–2048 (2016). doi:10.1080/00223131.2016.1199333

[7] A. Kishimoto, J. Kataoka, T. Nishiyama et al., Performance and field tests of a handheld Compton camera using 3-D position-sensitive scintillators coupled to multi-pixel photon counter arrays. J. Instrum. **9**(11), P11025–P11025 (2014). doi:10.1088/1748-0221/9/11/p11025

[8] Z. Toneva, S. Ivanov, G. Georgiev et al., Study of a small scale position-sensitive scintillator detector for γ-ray spectroscopy. J. Instrum. **15**(01) (2020). doi:10.1088/1748-0221/15/01/c01013

[9] J. Paul, P. Mandrou, J.Ballet et al., SIGMA: The hard X-ray and soft gamma-ray telescope on board the GRANAT space observatory. Adv. Space. Res. **11**(8), 289–302 (1991). doi:10.1016/0273-1177(91)90181-i

[10] F. Lebrun, J.P. Leray, P. Lavocat et al., ISGRI: the INTEGRAL Soft Gamma-Ray Imager. Astron. Astrophys. **411**(1), L141–L148 (2003). doi:10.1051/0004-6361:20031367

[11] S.R. Gottesman, E.E. Fenimore, New family of binary arrays for coded aperture imaging. Appl. Opt. **28**(20), 4344 (1989). doi:10.1364/ao.28.004344

[12] S.F. Sun, Z.M. Zhang, L. Shuai et al., Development of a panorama coded-aperture gamma camera for radiation detection. Radiat. Meas. **77**, 34–40 (2015). doi:10.1016/j.radmeas.2015.04.014

[13] E.E. Fenimore, T.M. Cannon, Coded aperture imaging with uniformly redundant arrays. Appl. Opt. **17**(3), 337 (1978). doi:10.1364/AO.17.000337

[14] S. Takyu, F. Nishikido, E. Yoshida et al., GAGG–MPPC detector with optimized light guide thickness for combined Compton-PET applications. Nucl. Instrum. Meth. A. **990**, 164998 (2021). doi:10.1016/j.nima.2020.164998

[15] I. Kuvvetli, C. Budtz-Jørgensen, A. Zappettini et al., A 3D CZT high resolution detector for x- and gamma-ray astronomy. Proc. SPIE. (2014). doi:10.1117/12.2055119

[16] E. Muñoz, J. Barrio, A. Etxebeste et al., Performance evaluation of MACACO: a multilayer Compton camera. Phys. Med. Biol. **62**(18), 7321–7341 (2017). doi:10.1088/1361-6560/aa8070

[17] D. Turecek, J. Jakubek, E. Trojanova et al., Single layer Compton camera based on Timepix3 technology. J. Instrum. **15**(01), (2020). doi:10.1088/1748-0221/15/01/c01014

[18] Y.L. Liu, J.Q. Fu, Y.L. Li et al., Preliminary results of a Compton camera based on a single 3D position-sensitive CZT detector. Nucl. Sci. Tech. **29**(10), (2018). doi:10.1007/s41365-018-0483-0

[19] W. Lu, L. Wang, Y. Yuan et al., Monte Carlo simulation for performance evaluation of detector model with a monolithic LaBr3(Ce) crystal and SiPM array for γ radiation imaging. Nucl. Sci. Tech. **33**(8) (2022). doi:10.1007/s41365-022-01081-3

[20] J. Kataoka, A. Kishimoto, T. Fujita et al., Recent progress of MPPC-based scintillation detectors in high precision X-ray and gamma-ray imaging. Nucl. Instrum. Meth. A **784**, 248–254 (2015). doi:10.1016/j.nima.2014.11.004

[21] H. Lee, J. Park, W. Lee, Development of modified scintillator-based single-crystal position-sensitive 4π Compton camera for a portable radiation imaging device. Nucl. Instrum. Meth. A **1043**, 167485 (2022). doi:10.1016/j.nima.2022.167485

[22] J.P. Zhang, C.M. Li, X.Y. Pang et al., Development of a 3-D Scintillator Detector for Compton Imaging Based on Laser Engraving. IEEE T. Nucl. Sci. **67**(7), 1691–1698 (2019). doi:10.1109/tns.2019.2956180
[23] Y.F. Hu, P. Fan, Z.L. Lyu et al., Design and performance evaluation of a 4π-view gamma camera with mosaic-patterned 3D position-sensitive scintillators. Nucl. Instrum. Meth. A **1023**, 165971 (2021). doi:10.1016/j.nima.2021.165971
[24] S. Watanabe, T. Tanaka, K. Nakazawa et al., A Si/CdTe semiconductor Compton camera. IEEE T. Nucl. Sci. **52**(5), 2045–2051 (2005). doi:10.1109/tns.2005.856995
[25] J.P. Zhang, X.Z. Liang, J.L. Cai et al., Prototype of an array SiPM-based scintillator Compton camera for radioactive materials detection. R.D.T.M. **3**(3) (2019). doi:10.1007/s41605-019-0095-1
[26] M.H. Dong, Z.Y. Yao, Y.S. Xiao et al., Development and preliminary results of a large-pixel two-layer LaBr3 Compton camera prototype. Nucl. Sci. Tech. **34**(8) (2023). doi:10.1007/s41365-023-01273-5
[27] K. Vetter, R. Barnowksi, A. Haefner et al., Gamma-Ray imaging for nuclear security and safety: Towards 3-D gamma-ray vision. Nucl. Instrum. Meth. A **878**, 159–168 (2017). doi:10.1016/j.nima.2017.08.040
[28] C. Zhao, B. Zhu, M. Zhao et al., Development of a modular high-sensitivity high-uniformity gamma camera for radiation monitoring applications. Nucl. Instrum. Meth. A **1003**, 165340 (2021). doi:10.1016/j.nima.2021.165340
[29] X.Z. Liang, L. Shuai, Y.T. Liu et al., Coded aperture and Compton imaging capability of spherical detector system design based on GAGG scintillators: A Monte Carlo study. Nucl. Instrum. Meth. A **1044**, 167503 (2022). doi:10.1016/j.nima.2022.167503
[30] Z.Q. Yuan, D.Y. Xue, H. Yang et al., A novel Compton camera with an annular absorber for enhancing the imaging efficiency in regions directly ahead: A simulation study. J. Nucl. Sci. Technol. doi:10.1080/00223131.2023.2207260
[31] R.Y. Wu, C.R. Geng, F. Tian et al., GPU-accelerated three-dimensional reconstruction method of the Compton camera and its application in radionuclide imaging. Nucl. Sci. Tech. **34**(4) (2023). doi:10.1007/s41365-023-01199-y
[32] R. Zhang, X.B. Tang, P. Gong et al., Low-noise reconstruction method for coded-aperture gamma camera based on multi-layer perceptron. Nucl. Eng. Technol. **52**(10), 2250–2261 (2020). doi:10.1016/j.net.2020.03.024
[33] J.X. Wen, X.T. Zheng, H.Z. Gao et al., Optimization of Timepix3-based conventional Compton camera using electron track algorithm. Nucl. Instrum. Meth. A **1021**, 165954 (2021). doi:10.1016/j.nima.2021.165954
[34] Q. Liu, Y. Cheng, X.G. Tuo et al., Neural network method for localization of radioactive sources within a partially coded field-of-view in coded-aperture imaging. Appl. Radiat. Isotopes. **170**, 109637 (2021). doi:10.1016/j.apradiso.2021.109637
[35] G.F. Knoll, Radiation Detection and Measurement, 4th edn. (Wiley, New York, 1979)
[36] A.J. Court, A.J. Dean, M. Yearworth et al., A position sensitive detector using a NaI(Tl)/photomultiplier tube combination for the energy range 200 keV to 10 MeV. Nucl. Instrum. Meth. A **273**(2–3), 706–710 (1988). doi:10.1016/0168-9002(88)90083-6
[37] G. Boella, A. Bussini, R.C. Butler et al., The basic unit of the imaging plane of the ZEBRA low energy gamma ray telescope. IEEE T. Nucl. Sci. **33**(1), 755–758 (1986). doi:10.1109/tns.1986.4337208
[38] C. Labanti, M. Marisaldi, F. Fuschino et al., Design and construction of the Mini-Calorimeter of the AGILE satellite. Nucl. Instrum. Meth. A **598**(2), 470–479 (2008). doi:10.1016/j.nima.2008.09.021
[39] F. Ur-Rehman, A.L. Goertzen, Calibration of Dual-Ended Readout of Axially Oriented 100-mm-Long LYSO Crystals for Use in a Compact PET System. IEEE T. Nucl. Sci. **59**(3), 561–567 (2012). doi:10.1109/tns.2012.2191978
[40] L.C. Parra, Reconstruction of cone-beam projections from Compton scattered data. IEEE T. Nucl. Sci. **47**(4), 1543–1550 (2000). doi:10.1109/23.873014
[41] M. Frandes, B. Timar, D. Lungeanu et al., Image Reconstruction Techniques for Compton Scattering Based Imaging: An Overview. Curr. Med. Imaging Rev. **12**(2), 95–105 (2016). doi:10.2174/1573405612666160128233916
[42] P. Fan, T. Ma, Q. Wei et al., Choice of crystal surface finishing for a dual-ended readout depth-of-interaction (DOI) detector. Phys. Med. Biol. **61**(3), 1041–1056 (2016). doi:10.1088/0031-9155/61/3/1041
[43] A. Levin, C. Moisan, A more physical approach to model the surface treatment of scintillation counters and its implementation into detect. IEEE Nucl. Sci. Conf. R. **2**, 1082–3654 (1996). doi:10.1109/NSSMIC.1996.591410
[44] M. Ablikim, Z.H. An, J.Z. Bai et al., Design and construction of the BESIII detector. Nucl. Instrum. Meth. A **614**(3), 345–399 (2010). doi:10.1016/j.nima.2009.12.050
[45] Y. Shao, R. Yao, T. Ma et al., A novel method to calibrate DOI function of a PET detector with a dual-ended-scintillator readout. Med. Phys. **35**(12), 5829–5840 (2008). doi:10.1118/1.3021118
[46] V. Schoenfelder, U. Graser, R. Diehl, Properties and performance of the MPI balloon-borne Compton telescope. Astron. Astrophys. **110**, 138–151 (1982). doi:10.1051/0004-6361/1982110138
[47] J.Q. Jia, J.L. Jiang, K. Liang et al., EQR SiPM with P-on-N diode configuration. Nucl. Sci. Tech. **30**, 119 (2019). doi:10.1007/s41365-019-0644-9
[48] F. Zhang, C. Herman, Z. He, Characterization of the H3D ASIC Readout System and 6.0 cm^3 3-D Position Sensitive CdZnTe Detectors. IEEE T. Nucl. Sci. **59**(1), 236–242 (2012). doi:10.1109/tns.2011.2175948